Delft University of Technology

Optical Hydrogen Sensing Materials for Applications at Sub-Zero Temperatures

Yuan, Ziqing; Schreuders, Herman; Dankelman, Robert; Dam, Bernard; Bannenberg, Lars J.

Important note
To cite this publication, please use the final published version (if applicable).
Please check the document version above.

Optical Hydrogen Sensing Materials for Applications at Sub-Zero Temperatures

*Ziqing Yuan, Herman Schreuders, Robert Dankelman, Bernard Dam,
and Lars J. Bannenberg**

Optical hydrogen sensors have the power to reliably detect hydrogen in an inherently safe way, which is crucial to ensure safe operation and prevent emissions of hydrogen as an indirect greenhouse gas. These sensors rely on metal hydride material that can reversibly absorb hydrogen when it is present in the environment, and as a result, change their optical properties. To apply this technology along hydrogen infrastructure, in hydrogen-powered planes and other vehicles, it is crucial that these sensors can operate down to −60 °C, a challenge so far unaddressed. Here, it is showed that metal hydride hydrogen sensing materials can be used to detect hydrogen optically down to −60 °C in just a couple of seconds and across a hydrogen concentration range of 0.02–100% with a 1% change in transmission per order of magnitude change in hydrogen concentration. The in-situ X-ray diffraction and optical transmission measurements show that Ta, $Ta_{88}Pd_{12}$, $Ta_{88}Ru_{12}$, and $Pd_{60}Au_{40}$ can gradually, reversibly and hysteresis-free absorb hydrogen while providing sufficient optical contrast. Specifically, $Ta_{88}Ru_{12}$ possesses the largest optical contrast and the swiftest response down to 6 s at −60 °C. These results confirm the operational viability and foretell new applications of metal hydride hydrogen sensing in cold conditions.

1. Introduction

Hydrogen has been hailed as a green energy carrier for the future and is considered to be a key component in the transition to a net CO_2 neutral society.[1–3] Characterized by its exceptional energy density and clean combustion, hydrogen is an ideal alternative to fossil fuels, with the potential to reduce greenhouse gas emissions and alleviate environmental stress.[4] As industry and the transportation sector increasingly move toward hydrogen-based

technologies, ensuring the safe handling and control of hydrogen has become a top priority. Indeed, mixtures of hydrogen and air can be flammable or even explosive at concentrations of 4–75% by volume, making the detection of leakage at an early stage vital. On top of that, hydrogen, when released into the atmosphere, can indirectly contribute to the greenhouse effect as it prolongs the lifetime of other greenhouse gasses such as methane.[5,6] In applications such as hydrogen-powered vehicles, airplanes, and near liquid hydrogen storage facilities, hydrogen sensors need to be able to operate both at room and sub-zero temperatures down to −60 °C i.e., slightly lower than the lowest temperature encountered during flights and in artic regions.

Conventional hydrogen sensing methods based on catalytic or thermal conduction face several limitations. For instance, catalytic sensors operate based on gas combustion on a catalytic surface and rely on the presence of oxygen for effective detection, making them unsuitable in low-oxygen environments, such as in airplanes.[7–10] Thermal conductivity sensors that measure the thermal conductivity of gas mixtures by comparing them to a reference are sensitive to environmental changes, particularly gas flow rates.[11] Moreover, both sensor types have a relatively high detection limit, making the detection of small leaks hardly possible. As such, this calls for alternative hydrogen sensors.[9,10,12–14]

Optical metal hydride hydrogen sensors have emerged as a promising alternative to overcome the above-mentioned challenges of hydrogen sensing. These sensors utilize the unique properties of metal–organic frameworks,[15] oxides,[16,17] or metal hydrides. In the latter case, the metal hydride can reversibly absorb and release hydrogen when exposed to a hydrogen-containing environment. In turn, the absorption of hydrogen by the metal hydride results in measurable changes in its optical properties. By measuring e.g. the changes in optical transmission or reflectivity, the hydrogen concentration/partial hydrogen pressure may then be determined. This method greatly increases the safety and sensitivity of hydrogen sensing as it does not require any current around the sensing area.[18–25]

The performance of an optical hydrogen sensor is directly related to the properties of the hydrogen sensing material. As a hydrogen sensing material, palladium has been a frequent choice.

Z. Yuan, H. Schreuders, R. Dankelman, B. Dam, L. J. Bannenberg
Faculty of Applied Sciences
Delft University of Technology
Mekelweg 15, Delft 2629, The Netherlands
E-mail: l.j.bannenberg@tudelft.nl

**ADVANCED
SCIENCE NEWS**

www.advancedsciencenews.com

**ADVANCED
FUNCTIONAL
MATERIALS**

www.afm-journal.de

Palladium can readily catalyze the dissociation of molecular hydrogen present in the atmosphere into atomic hydrogen that can be absorbed by the material, and features a modest sensing range at room temperature of 3 orders of magnitude.[23,24,26–29] However, hysteresis arising from the first-order phase transition upon hydrogen sorption makes the sensor's response depend on the hydrogen concentration/pressure history. In other words, there is no longer a one-to-one relationship between the optical property and the hydrogen concentration. To increase the sensitivity at low hydrogen concentrations and suppress the unwanted phase transition and thus the hysteresis, Pd has been alloyed by elements including Au, which at sufficiently high concentrations can suppress the undesired phase transition at the expense of a significantly reduced optical contrast.[23,24,26–30] As an alternative to Pd-based sensing materials, tantalum-based hydrogen sensing have emerged.[31,32] When combined with a suitable catalyst to promote hydrogen dissociation, these materials feature a sensing range of at least 7 orders in magnitude in partial hydrogen pressure/hydrogen concentration that is completely reversible and free of any hysteresis, and can provide sub-second response times. This sensing range and the desired sensitivity of the sensor can be further tuned by alloying tantalum with elements such as Pd[33] and Ru.[34]

Despite extensive testing at room temperature, no optical metal hydride hydrogen sensors have yet been proven to operate at sub-zero temperatures. Hydrogen absorption is challenging at these lower temperatures due to the slowing of critical processes such as hydrogen molecule dissociation, chemisorption, and diffusion.[35–38] These processes are essential for efficient hydrogen sorption kinetics, and their rate is expected to decrease exponentially with decreasing temperature in accordance with Arrhenius' law.[39] This results in a delayed sensor response to a change in the hydrogen concentration.

Low temperatures also impact the sensing range of materials in optical metal hydride hydrogen sensors. These materials must provide a suitable optical contrast, which may shift toward lower partial hydrogen pressures or, equivalently, hydrogen concentrations. In these hydrogen sensors, the detection of hydrogen is achieved by monitoring the refractive index change, which correlates with the amount of hydrogen absorbed by the sensing material typically denoted by the hydrogen-to-metal ratio (H/M).[34] For a given H/M ratio, the equilibrium partial hydrogen pressures shift with decreasing temperature T to lower partial hydrogen pressures P_{H2} according to Van 't Hoff's law:

$$\ln\left(\frac{P_{H2}}{P_0}\right) = \frac{\Delta H}{RT} - \frac{\Delta S}{R} \tag{1}$$

where ΔH and ΔS are the enthalpy and entropy of hydrogenation for a specific H/M ratio, respectively, P_0 the standard pressure, and R the gas constant. For a metal hydride hydrogen sensing material, ΔH is on the order of -10 to -100 kJ/mol$_{H_2}$, while ΔS is typically around -130 J/K·mol$_{H_2}$.[40] As ΔH is negative, reducing the temperature makes the term $\frac{\Delta H}{RT}$ a larger negative number. Consequently, P_{H2} shifts to lower equilibrium pressures. At a given hydrogen pressure, the hydrogen concentration within the metal increases as the temperature decreases. This is accompanied by a slowdown in hydrogen dissociation and diffusion, meaning the material will take longer to reach equilibrium. Ad-

ditionally, the larger volume expansion due to the accommodation of more hydrogen atoms increases the possibility of phase transitions or even plastic deformation.

At low temperatures, phase transitions that are normally suppressed by alloying or nanoconfinement at room temperature can emerge.[30,33,41–44] For instance, alloying Pd with Au shifts the temperature above which no metal-to-metal hydride phase transition occurs (i.e., the critical temperature) from about 290°C toward lower temperatures.[19,45] In Ta-based films, nanoconfinement is used to suppress the critical temperature of about 61°C reported for bulk materials.[46,47] At lower temperatures, these first-order phase transitions may no longer be suppressed, introducing hysteresis into the sensing response.

The primary objective of this research is to investigate the performance of hydrogen sensing materials at temperatures down to -60 °C. For this research, we selected four frequently considered hydrogen-sensing materials that exhibit no hysteresis at room temperature: Pd$_{60}$Au$_{40}$, Ta, Ta$_{88}$Ru$_{12}$, Ta$_{88}$Pd$_{12}$. As illustrated in **Figure 1**, a layer of 20 nm of these materials have been combined with a 4 nm Ti adhesion/seed layer,[48] and, in the case of the Ta (alloys), a 5 nm Pd$_{60}$Au$_{40}$ capping layer was used to prevent oxidation and catalyze the hydrogen dissociation reaction. The samples also include a 30 nm polytetrafluoroethylene (PTFE) polymer protective coating, of which previous studies have shown that it provides protection against cross-sensitivity to other chemical species and that it can accelerate the hydrogenation kinetics.[49–52] We fabricated these materials by magnetron sputtering, a commonly used technique to deposit hydrogen sensing materials as it is environmentally benign, scalable and compatible with depositions on substrates and optical fibers. Using in-situ X-ray diffraction (XRD) and optical transmission measurements, we demonstrate that all these hydrogen sensing materials exhibit remarkable efficacy in detecting hydrogen even at low temperatures, showcasing hysteresis-free performance down to -60 °C. All four materials have a suitable optical contrast allowing hydrogen detection within the range of 0.002 $< C_{H2} <$ 100%. Amongst the sensing materials studied, Ta$_{88}$Ru$_{12}$ showcases the largest optical contrast at -60 °C while also providing the shortest response time enabling the detection of 3% hydrogen within a mere 6 s at -60 °C. Additionally, our analysis at low temperatures identifies surface effects such as hydrogen dissociation as the rate-limiting factor. Taken together, these results show that metal hydride based optical hydrogen sensors can be used at temperatures as low as -60 °C, opening new avenues for practical applications in cold environments.

2. Experimental Section

2.1. Sample Fabrication

The samples, illustrated in Figure 1, are thin films on 10 × 10 mm² quartz substrates with a thickness of 0.5 mm and surface roughness <0.4 nm (Mateck GmbH, Jülich, Germany). All layers were deposited by magnetron sputtering in an ultrahigh vacuum chamber (AJA Int., Hingham, MA, United States of America) with a base pressure of 10^{-6} Pa. A schematic representation of the deposition set-up is available in Figure S1 (Supporting Information). The targets have a diameter of 5.08 cm (2 in.) and a purity of at least 99.9% (Mateck GmbH, Jülich, Germany). The deposition
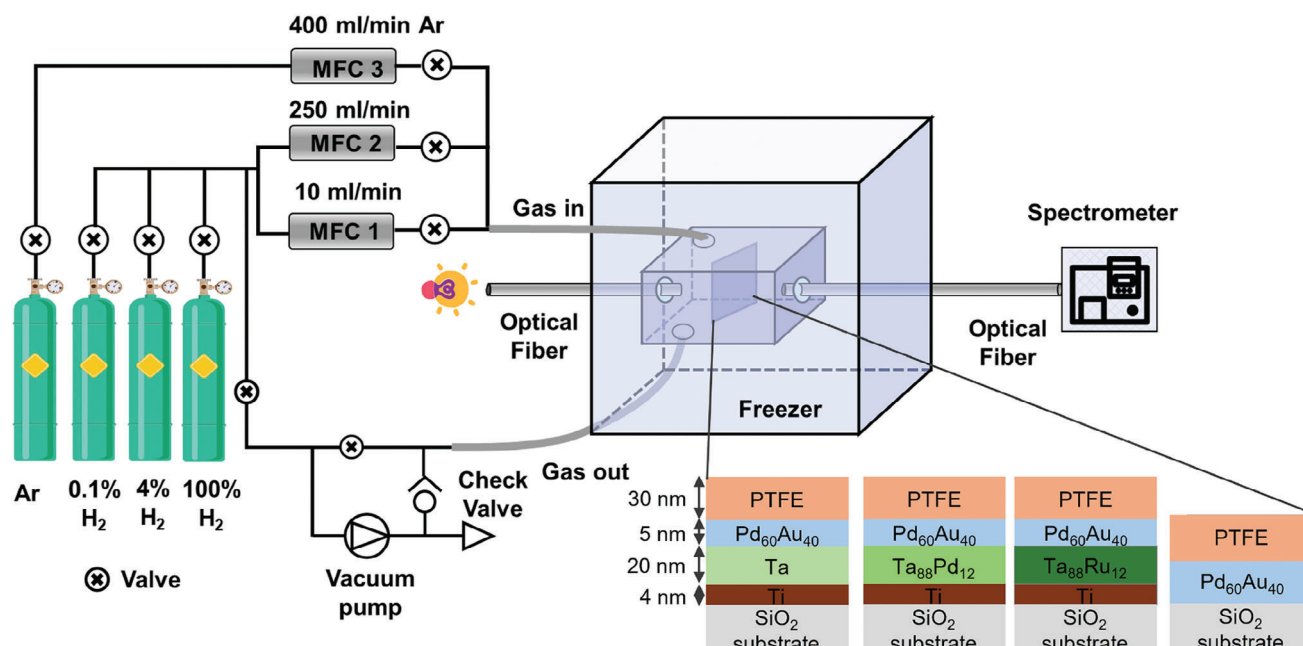
Figure 1. Schematic diagram of the experimental configuration designed for quantifying the change in transmittance of metal hydride thin films when subjected to varying hydrogen concentrations at low temperatures. The inset shows a schematic representation of the samples.

was performed under 0.3 Pa of Ar. The unheated substrates were rotated during the deposition to enhance the homogeneity of the layers. For the thin film alloys, two targets were co-sputtered and the direct current (DC) power supply was adjusted to achieve the desired compositions. Typical deposition rates include 0.14 nm s^{-1} (130 W DC) for Ta, 0.41 nm s^{-1} (50 W DC) for Ru, 0.047 nm s^{-1} (150 W DC) for Ti, 0.11 nm s^{-1} (50 W DC) for Pd, 0.10 nm s^{-1} (30 W DC) for Au. PTFE was prepared by radiofrequency magnetron sputtering at 70 W yielding a typical deposition rate of 0.029 nm s^{-1}. The exact deposition conditions are reported in Table S1 (Supporting Information). The crystal structure of all samples was verified with XRD, and X-ray reflectometry (XRR) was used to obtain estimates of the layer thickness, roughness, and density for each layer composing the thin films, both before and after exposure to hydrogen. (Figures S2–S8 and Tables S2 and S3, Supporting Information). These measurements show that also after exposure to hydrogen the layered structure and crystal structure of the material is maintained, indicated good mechanical stability. In addition, X-ray photoelectron spectroscopy measurements were performed to study the composition of the top PTFE coating (Figure S13, Supporting Information). Similar to previous experiments, these measurements revealed the presence of C-CF, CF, CF_2, and CF_3 bonds.[49–51] Atomic force microscopy measurements of the film reveal that the peak-to-valley roughness of the Ta sample is slightly larger than the $Pd_{60}Au_{40}$ sample (Figure S14, Supporting Information).

2.2. Structural Measurements

To assess the structural behavior at low temperatures down to −60 °C, for the first time a tailor-made in-situ XRD sample environment that allows measurements at low temperatures and un-

der a controllable hydrogen atmosphere is constructed. The set-up, which is schematically illustrated in Figure S15 (Supporting Information), consists of a TTK 450 low-temperature chamber with a base pressure of 10^{-3} mbar, equipped with liquid-nitrogen cooling (Anton Paar, Graz, Austria). The partial hydrogen pressure was varied by changing the absolute pressure of a 4% H_2 in He gas mixture (Linde Gas Benelux BV, Dieren, the Netherlands). The pressure is controlled using a pressure controller (MKS Type 250E, Andover, MA, USA) connected to a solenoidal inlet valve and measured using a MKS baratron manometer (MKS120AD, Andover, MA, USA). The flow was regulated using a mass flow controller (Bronkhorst F-201CV-200- AAD-33-V EL Flow Select 200 mln min^{-1} Ar). To enable sufficient flow at low pressures, a solenoidal outlet valve placed in parallel to the flow controller was opened partially. A Labview program running on a PC, controlled and recorded the gas pressure and flow during measurements. Further details on the pressure and flow regulation can be found in ref. [53].

The in-situ XRD measurements were performed in Bragg–Brentano geometry ($30 \leqslant 2\theta \leqslant 90°$) with a Panalytical X'pert diffractometer (Almelo, the Netherlands) equipped with a Cu–Kα source ($\lambda = 0.1542$ nm). At each temperature, the height was carefully aligned to account for thermal expansion of the sample holder/set-up. This was done by performing diffraction measurements around a diffraction peak and optimize for maximum intensity. The experimental XRD data was fitted to two pseudo-Voigt functions: one to account for the (110)-Ta reflection, and one for the (111)-$Pd_{60}Au_{40}$ reflection. This was done to accurately extract the peak position, which was, with the help of Bragg's law, used to obtain the d-spacing.

Room temperature XRR (Figures S2–S4, Supporting Information) and XRD (Figures S5–S8, Supporting Information) measurements were performed using a Bruker Discover

Diffractometer. The settings used for these measurements are the same as in Ref. [48]. The XRR data were fitted with GenX3[54,55] (Tables S2 and S3, Supporting Information).

2.3. Optical Measurements

Figure 1 depicts a schematic representation of the set-up newly designed to measure the optical transmission of the sensing materials as a function of the hydrogen pressure/concentration at temperatures of $-60 \leqslant T \leqslant 20$ °C. In essence, the setup consists of a pressure cell in which the sample is located. The pressure cell is positioned inside a temperature-controlled freezer (Elcold 11 Pro, Horby, Denmark). Two optical fiber feedthroughs are connected to the pressure cell, one of them transports light from the halogen light source (Ocean Optics HL-2000-FHSA) to the sample (Figure S16, Supporting Information), the other one collects the transmitted light and transports it to the Ocean Optics HR4000 spectrometer with a resolution of 0.025 nm (full width halve maximum). This enables to measure the intensity of transmitted light at various wavelengths. The changes in optical transmission with hydrogen exposure are analyzed by measuring the intensity of the transmitted light I_{H2} and first correcting it for the noise of the spectrometer by the intensity in the dark I_{Dark}. Subsequently, this intensity is normalized at the tested temperature to the intensity of the transmitted light $I_{0.002\%}$ (20 Pa) measured at $C_{H2} = 0.02\%$ to obtain the normalized changes of the optical transmission when exposed to a hydrogen concentration:

$$\frac{\mathcal{T}_{H2}}{\mathcal{T}_0} = \frac{I_{H2} - I_{Dark}}{I_{0.002\%} - I_{Dark}} \quad (2)$$

From the spectrum, light with a wavelength between 650 and 660 nm was selected for testing, as this range offers minimal noise and maximizes the intensity of the light source. Indeed, for this wavelength the spectrum of the used light source shows a maximum (Figure S16, Supporting Information), while the absolute optical transmission is also relatively high for these wavelengths (Figure S17, Supporting Information). To achieve the desired hydrogen concentration inside the cell, we mix pure argon gas from the gas network (5N purity) with either 4% and 100% H_2 in Ar (Linde Gas Benelux BV, Dieren, the Netherlands) using three flow controllers (GF040CXXC, Brooks Instruments, Hatfield PA, United States of America) placed in parallel and controlled with in-house developed Labview software. The hydrogen concentration C_{H2} can then be changed by setting the flows Q_{Ar} and Q_{H2} of the Argon and hydrogen-containing gas mixture selected with concentration C_{gas} according to:

$$C_{H2} = C_{gas} \frac{Q_{H2}}{Q_{H2} + Q_{Ar}} \quad (3)$$

The typical total gas flow during the measurements is 250 mL min^{-1}. The gas system's final outlet is connected to the exhaust port and is equipped with a check valve to ensure the pressure remains constant at 1 bar. Thorough evacuation of the gas lines and cell using a vacuum pump (Adixen Drytel 1025, Pfeiffer Vacuum, Aßlar, Germany) was carried out when transitioning between different gas cylinders ($P_{cell} < 10^{-3}$ mbar).

To ensure precise temperature monitoring within the cell, a K-type thermocouple temperature sensor was positioned inside the cell for real-time temperature data acquisition. Notably, the entire cell, along with a portion of the gas system, was housed within a refrigerated environment. Due to potential vibrational interference from the refrigeration cycles affecting the fiber optic calibration, experiments were conducted only when the freezer motor was switched off. It was verified that the average sample temperature throughout the experiment matched the intended target temperature within ± 2 °C.

To measure the response time, the partial pressure was varied stepwise by changing the absolute pressure of a pre-defined hydrogen-argon gas mixture. This was done using a pressure controller (MKS Type 250E, MKS Instruments, Andover, MA, United States of America) that is connected to a solenoidal inlet valve which adjusts the pressure. A pressure transducer (MKS Baratron) is included in the pressure controller to measure the actual pressure of the pressurized chamber. The change in optical transmission was measured upon a change in partial hydrogen pressure. The response time is defined as the time required to reach 90% of the new equilibrium state following a hydrogen pressure step. Between these pressure steps, the samples are subjected to at least 5 min at a reference pressure of 24 Pa, ensuring that each starting point of a pressure increase is at equilibrium.

3. Results

3.1. Structural Behavior

For hydrogen sensing materials it is important that no (first order) phase transition or plastic deformation is present when they are exposed to hydrogen. Phase transitions, as well as plastic deformation of the metal hydride, result in a hysteretic and slower response and may render the material unstable over repeated exposure to hydrogen.[46] Unlike its bulk counterpart that shows a series of phase transitions below its critical temperature of $T_c = 61$°C when exposed to hydrogen at room temperature, the tantalum and tantalum-alloy thin films do not show any signs of a phase transition but a gradual elastic expansion and deformation of the lattice.[56] Similarly, in $Pd_{100-y}Au_y$, Au suppresses the undesirable first-order metal-to-metal hydride phase transition present in pure Pd.[30] To investigate whether the hysteresis remains suppressed at low temperatures, we performed in-situ X-ray diffraction measurements while exposing the film to hydrogen at temperatures down to −60 °C.

Figure 2 presents the XRD results. As the films are highly textured with the (110) of the Ta-based sensing materials and the (111) of the $Pd_{60}Au_{40}$ in the out-of-plane direction, we focus our attention to these reflections. Full diffraction patterns can be found in Figures S9–S12 (Supporting Information). We find two almost overlapping diffraction peaks: the (110) diffraction peak of the $Ta_{88}Ru_{12}$ sensing layer and the (111) peak of the $Pd_{60}Au_{40}$ capping layer at $2\theta = 39.3°$. With increasing partial hydrogen pressures, the (110) $Ta_{88}Ru_{12}$ diffraction peak continuously shifts to lower diffraction angles. This indicates that a gradual lattice expansion occurs as hydrogen is absorbed by the material.

Most importantly, for all hydrogen sensing materials studied, no additional diffraction peak emerges when the material is exposed to hydrogen, meaning that no phase transition related
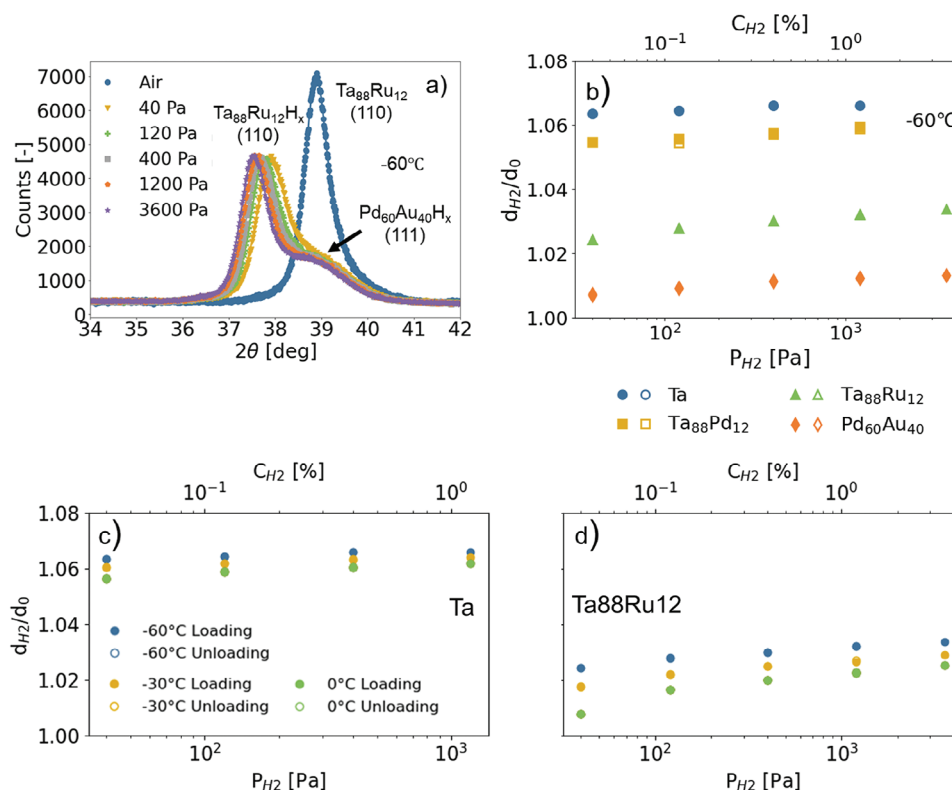
**ADVANCED
SCIENCE NEWS**

www.advancedsciencenews.com

**ADVANCED
FUNCTIONAL
MATERIALS**

www.afm-journal.de

Figure 2. Temperature and partial hydrogen pressure (concentration) dependent X-ray diffraction measurements. a) In situ X-ray diffraction patterns of a 20 nm $Ta_{88}Ru_{12}$ thin film, with a 4 nm Ti adhesion layer and capped with a 5 nm $Pd_{60}Au_{40}$ layer that is covered with a 30 nm PTFE for the partial hydrogen pressures indicated in the legend and measured at −60 °C. The continuous lines represent fits of two pseudo-Voigt functions to the experimental data. b) Partial hydrogen pressure dependence of the expansion of the d_{110}-spacing Ta, $Ta_{88}Pd_{12}$, $Ta_{88}Ru_{12}$, and the d_{111}-spacing in $Pd_{60}Au_{40}$ measured at −60 °C. The d-spacing is normalized to the d-spacing when no hydrogen is in the environment, d_0. d_{hkl} is obtained by fitting the XRD data of Figures S18–S21 (Supporting Information). The fitted peak position is converted to d_{hkl} using Bragg's law. The open (closed) symbols indicate measurements performed after decreasing (increasing) the partial hydrogen pressure. (c) and (d) Temperature and partial hydrogen pressure dependence of the d_{110}-spacing expansion of a Ta and $Ta_{88}Ru_{12}$, respectively. Data on $Ta_{88}Pd_{12}$ and $Pd_{60}Au_{40}$ is provided in Figure S22 (Supporting Information).

to hydrogen absorption occurs, even at temperatures as low as −60 °C (Figures S18–S21, Supporting Information). As the critical temperature of TaH_x is 61°C for bulk material[19,31] this implies that the nano-confinement of tantalum can successfully suppress any phase transition even at temperatures as low as −60 °C.

As a next step, we calculated the relative change in d-spacing d_{H2}/d_0 of the material after hydrogen exposure where d_{H2} is the d-spacing in the presence of hydrogen and d_0 is the d-spacing of the sample that is completely unloaded. The d-spacing refers to the distance between atomic planes in a crystal lattice and is calculated based on the fitted peak position of the diffraction peaks and Bragg's law. Figure 2b shows the d-spacing change after stepwise increases in partial hydrogen pressure for all samples at −60 °C, while Figure S22 (Supporting Information) presents the d-spacing under similar conditions in the temperature range of 0 to −60 °C. The results in Figure 2b indicate a gradual and elastic expansion of the unit cell with increasing partial hydrogen pressure at −60 °C. As the d-spacing remains identical after increasing and decreasing pressure steps, as shown in both figures, no hysteresis is observed. This is an important result as it implies that a hysteresis-free hydrogen sensor can be made even at temperatures down to −60 °C.

Comparing the expansion of the samples at P_{H2} = 40 Pa at −60 °C, we observe that this is the largest for Ta (6.4%), followed by 5.7% for $Ta_{88}Pd_{12}$, 2.4% for $Ta_{88}Ru_{12}$ and about 1.5% for $Pd_{60}Au_{40}$. The decrease in the expansion with Pd and Ru is consistent with previous research that shows that elemental substitution of Ta by alloys can successfully compress the unit cell, shifting the pressure-composition-isotherms to higher hydrogen pressures. In addition, it is consistent with the earlier findings that this effect is larger for the substitution of Ta by Ru[34] than by Pd.[33]

Within the partial pressure window $10^{+2} < P_{H2} < 10^{+4}$ Pa, i.e., the explosive limit of hydrogen in air concentration of C_{H2} = 4% (P_{H2} = 4,000 Pa), we observe that the largest change in lattice expansion *within* this window is realized for $Ta_{88}Ru_{12}$. This composition exhibits a change in d_{H2}/d_0 from 1.024 to 1.033, which is three times larger than the corresponding change observed for the Ta sample (from 1.064 to 1.067 at −60 °C). This difference indicates a potentially larger sensitivity of $Ta_{88}Ru_{12}$ as a hydrogen-sensing material compared to Ta within the investigated pressure range. Indeed, a larger change in lattice expansion corresponds, ceteris paribus, to a larger change in hydrogen-to-metal ratio, and possibly thus in a large change of the optical transmission.
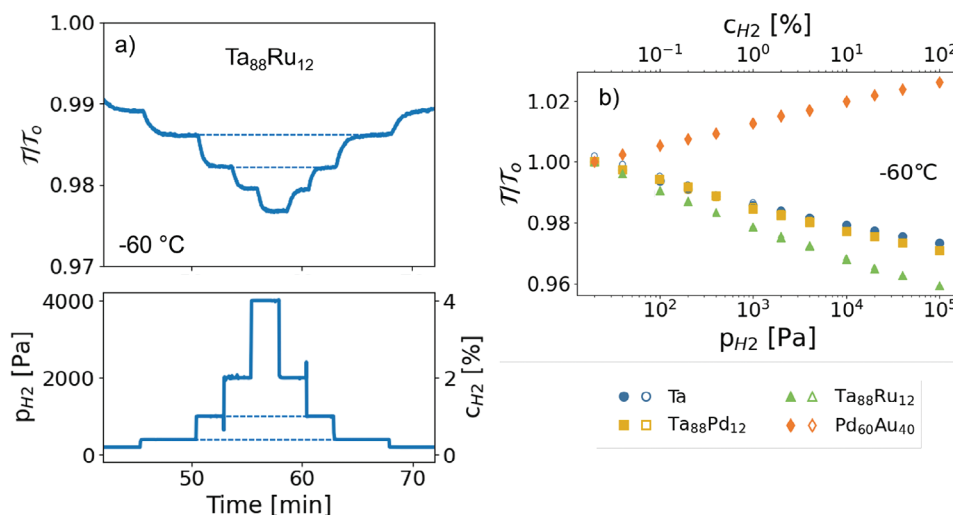
**ADVANCED
SCIENCE NEWS**

www.advancedsciencenews.com

**ADVANCED
FUNCTIONAL
MATERIALS**

www.afm-journal.de

Figure 3. Hydrogen concentration dependence of the optical transmission $\mathcal{T}$ at wavelengths 650–660 nm at −60 °C. a) Changes of the optical transmission of a 20 nm $Ta_{88}Ru_{12}$ thin film, with a 4 nm Ti adhesion layer capped with a 5 nm $Pd_{60}Au_{40}$ layer that is covered with a 30 nm PTFE layer as a function of time during which the partial hydrogen pressure/concentration is stepwise varied. The top panel shows the optical transmission normalized to the optical transmission of the sample at the reference hydrogen pressure $\mathcal{T}_0$ of 20 Pa (0.02%). The bottom panel shows the corresponding partial hydrogen pressure/concentration as a function of time. b) Partial hydrogen pressure dependence of the optical transmission relative to the transmission of the sample at reference hydrogen pressure 20 Pa for a 20 nm Ta, $Ta_{88}Pd_{12}$, $Ta_{88}Ru_{12}$, with a 4 nm Ti adhesion layer and capped by a 5 nm $Pd_{60}Au_{40}$ layer covered with a 30 nm PTFE layer, and the 20 nm $Pd_{60}Au_{40}$ thin film covered with a 30 nm PTFE layer, as measured by both stepwise increasing (closed symbols) and decreasing the pressure (open symbols). We note that the overlap of the increasing and decreasing data is large.

Furthermore, Figure 2c,d and Figure S22 (Supporting Information) show that the absolute d-spacing increases for a given partial hydrogen pressure with decreasing temperature. For the materials studied here, we determined before that the d-spacing at room temperature is directly related to the H/M ratio.[26,33,34] Accordingly, we observe in agreement with Van 't Hoff's law (Equation 1), a large d-spacing at a specific P_{H2} for lower temperatures. Moreover, these figures also indicate that the slope of the d-spacing expansion with respect to P_{H2} is substantially reduced when the temperature is lowered. Here, sensitivity refers to the degree of change in the d-spacing of the material in response to variations in P_{H2}. Hence, the sensitivity of the sensing materials substantially decreases with decreasing temperature, which we further study in the next section with optical transmission measurements.

3.2. Optical Response

An ideal material for optical hydrogen sensing should exhibit a consistent and steady alteration of its optical characteristics across a broad range of hydrogen pressures with a response that is not influenced by the sensor's previous pressure exposures (hysteresis-free). To study the optical response of the sensing materials under different partial hydrogen pressures and temperatures, we study the changes in red-light optical transmission (650 $< \lambda <$ 660 nm) and normalize the optical response at $C_{H2} = 0.02\%$ according to Equation (2).

As an illustrative example, **Figure 3a** presents the normalized optical transmission for $Ta_{88}Ru_{12}$ as a function of time during which the partial hydrogen pressure was stepwise increased and subsequently decreased. It shows that the stepwise changes of the partial hydrogen pressure result in well-defined steps in the optical transmission that are stable over time and completely free of hysteresis. Indeed, the optical transmission is within the experimental accuracy the same after increasing and decreasing pressure steps. The spikes observed in the pressure profile are attributed to the response of the pressure controller and have a duration of max 2 s.

Figure 3b summarizes the change in optical transmission at −60 °C with a change in hydrogen concentration for both $Ta_{88}Ru_{12}$ as well as the three other compositions. The plotted transmission values represent the stable optical transmission after each increase or decrease in partial hydrogen pressure, as illustrated in Figure 3a. Most importantly, the figure demonstrates that the optical transmission remains the same after both increasing and decreasing pressure steps, indicating no hysteresis across the entire studied pressure range, even at temperatures as low as −60 °C. These findings are consistent with the XRD results in Figure 2 and Figure S22 (Supporting Information), which also show no signs of phase transitions or hysteresis in the d-spacing's dependence on partial hydrogen pressure. The resolution of these sensors, crucial for precise hydrogen concentration detection, is inferred from the slope of the $\mathcal{T}/\mathcal{T}_o$ curve against hydrogen pressure. Among the tested materials, $Ta_{88}Ru_{12}$ shows the steepest slope, indicating the highest resolution, which is essential for accurate performance at −60 °C. $Ta_{88}Ru_{12}$ and $Ta_{88}Pd_{12}$ exhibit changes in normalized transmission upon hydrogen exposure, with respective differences of 4% and 3%. This is consistent with previous research as alloying Ta with Ru (or Pd) compresses the unit cell of tantalum.[33,34] In turn, the Ru alloying shifts the sensor's operating range toward higher pressures, enhancing its sensitivity, particularly at lower temperatures, where the hydrogen-to-metal ratio in the material is closer to saturation
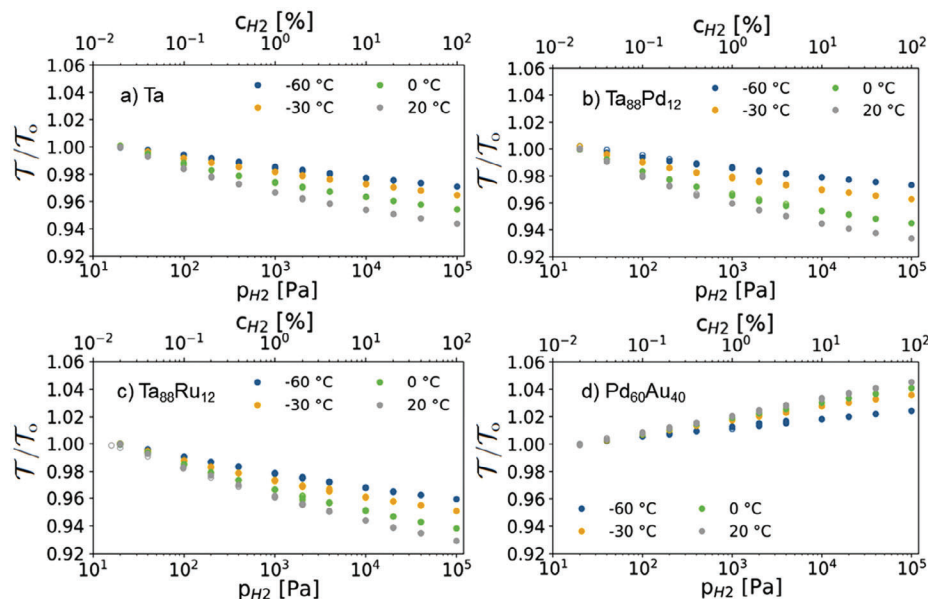
**ADVANCED
SCIENCE NEWS**

www.advancedsciencenews.com

**ADVANCED
FUNCTIONAL
MATERIALS**

www.afm-journal.de

Figure 4. Partial hydrogen pressure/hydrogen concentration dependence of the optical transmission $\mathcal{T}$ at wavelength 650–660 nm of a 20 nm a) Ta, b) $Ta_{88}Pd_{12}$, c) $Ta_{88}Ru_{12}$ thin films, each with a 4 nm Ti adhesion layer capped with a 5 nm $Pd_{60}Au_{40}$ layer that is covered with a 30 nm PTFE layer, and d) $Pd_{60}Au_{40}$ thin film covered with a 30 nm PTFE layer. All measurements are normalized relative to the transmission of the sample at a reference hydrogen pressure of 20 Pa and have been performed at the temperatures indicated in the figure legend.

than at higher temperatures. On the other hand, $Pd_{60}Au_{40}$ becomes more transparent upon hydrogen absorption but exhibits the smallest optical contrast across the entire range of hydrogen pressures.

The effect of temperature on the optical response of the thin films is shown in **Figure 4**. $Ta_{88}Ru_{12}$ demonstrates the largest change in transmission within the range $0.02 < C_{H2} < 100\%$. Within this range, a change of the optical transmission of approximately 4% is observed at $-60\,°C$ (i.e., $\mathcal{T}/\mathcal{T}_0$ drops from 1 to 0.96). This is slightly lower than the 5% change at $-30\,°C$ and considerably smaller than the 7.2% change observed at room temperature. Similar trends are observed for all materials, indicating that the sensitivity of the hydrogen-sensing materials, which is directly related to the slope of the graph of $\mathcal{T}/\mathcal{T}_0$ versus C_{H2}, decreases with decreasing temperatures.

Based on the optical measurements, $Ta_{88}Ru_{12}$ can be used to construct a sensor with the largest optical response. The relative sensitivity of the material is constant across the entire investigated sensing range of $0.02 \leqslant C_{H2} \leqslant 100\%$ with a 1% change in transmission per order of magnitude change in hydrogen concentration at $-60\,°C$. We note that the sensitivity can be further optimized by considering different wavelengths, layer thicknesses and light sources, and that the resolution of the sensor constructed from the sensing material will also depend on the noise/stability of the light source. Furthermore, we also note that the lowest hydrogen concentration that we detected was limited by the experimental set-up.

3.3. Response Time and Response Rate

An ideal material for optical hydrogen sensing should not only exhibit a high sensitivity but also a short response time. The latter

is crucial for ensuring the reliability and efficiency of hydrogen sensors, particularly in applications that require rapid detection of hydrogen leaks. This is especially important close to the explosive limit of 4% in air.

To ensure that the data primarily reflect the properties of the samples, we analyzed the response times of these samples, as well as the response time of the setup. In our subsequent analysis, we only included data where the response time of the sample was at least three times greater than that of the setup. To measure the response time, we changed the partial hydrogen pressure from a baseline of $P_{H2} = 24$ Pa (0.024%) to the partial hydrogen pressure of interest. We then define the response time as the time it takes to reach 90% of the final transmission. Examples of the normalized response time curves can be found in Figure S23 (Supporting Information).

Figure 5a presents the response time as a function of partial hydrogen pressure at $-60\,°C$ for the four samples under investigation. Among these, the $Ta_{88}Ru_{12}$ sample demonstrates the fastest response times among the materials tested, with response times as low as approximately 6 s at $C_{H2} = 3\%$. There is a strong hydrogen concentration dependence of the response time, which for $Ta_{88}Ru_{12}$ increases to 38 s at $C_{H2} = 0.08\%$. While $Ta_{88}Pd_{12}$ shows a similar response time as that of $Ta_{88}Ru_{12}$, the response times for Ta and especially $Pd_{60}Au_{40}$ are considerably longer and show a stronger dependence on pressure. As a result, at $C_{H2} = 0.4\%$, Ta exhibits a response time of 22 s, and $Pd_{60}Au_{40}$ shows 38 s, both significantly longer than the 15 s for $Ta_{88}Ru_{12}$ and 16 s for $Ta_{88}Pd_{12}$.

Figure 5b,c provides the partial hydrogen pressure dependence of the response times for Ta and $Pd_{60}Au_{40}$ sample at three different temperatures between $-60\,°C$ and $0\,°C$. Across all materials, a decrease in response time is observed with increasing temperature. For Ta, we see that the response time at $C_{H2} = 1.6\%$
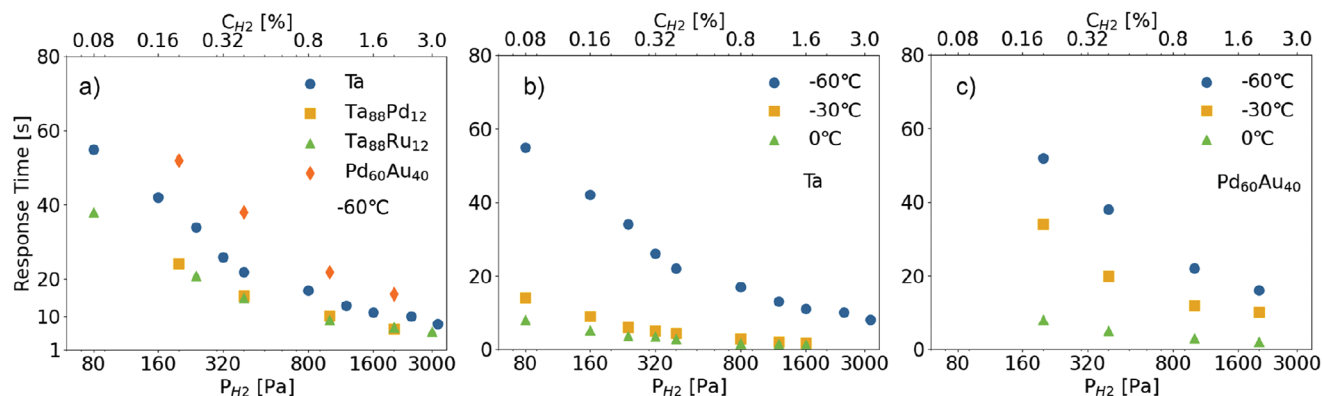
ADVANCED
SCIENCE NEWS

www.advancedsciencenews.com

ADVANCED
FUNCTIONAL
MATERIALS

www.afm-journal.de

Figure 5. a) Response time t_{90} as a function of partial hydrogen pressure for Ta, $Ta_{88}Pd_{12}$, $Ta_{88}Ru_{12}$, and $Pd_{60}Au_{40}$ at −60 °C. b,c) Response times as a function of partial hydrogen pressure at various temperatures for b) Ta and c) $Pd_{60}Au_{40}$.

drops from 11 s at −60 °C to 1.2 s at 0 °C, i.e., a factor of 10 faster. Such a temperature dependence is expected, as both the hydrogen dissociation reaction and hydrogen diffusion have a strong temperature dependence.

To further enhance the sensor's responsiveness, we need to understand the dynamics of the hydrogen absorption process, particularly the interplay between surface and thin film. Borgschulte et al. propose a two-step model that effectively captures this dynamic, where hydrogen absorption is governed by two key processes: the dissociation of hydrogen molecules on the metal surface and the subsequent diffusion of atomic hydrogen into the bulk material. The first step involves an energy barrier associated with the dissociation of molecular hydrogen (H_2) into atomic hydrogen on the surface, which requires sufficient active sites and favorable surface conditions. The second step involves the diffusion of hydrogen atoms into the bulk of the material, which is influenced by factors such as the material's structure and temperature.[38] If the response rate is found to be diffusion-limited, efforts should focus on enhancing hydrogen diffusion within the material. Conversely, if the surface dissociation process is the limiting factor, the priority should shift toward optimizing the surface properties, including increasing the number of active sites and reducing the activation energy required for dissociation.

One way to gain this understanding is by analyzing the dependence of the hydrogenation rate on partial hydrogen pressure. To calculate the hydrogenation rate, we use the relationship established in previous neutron reflectometry studies, which have shown that, for these materials, the logarithmic change in optical transmission $\Delta \ln(\mathcal{T}/\mathcal{T}_o)$ is proportional to the change in hydrogen concentration inside the material.[30,34,48] As a result, we can deduce that:

$$\text{Response Rate} \propto \frac{\Delta \ln(\mathcal{T}/\mathcal{T}_o)}{t_{90}} \qquad (4)$$

where $\Delta \ln(\mathcal{T}/\mathcal{T}_o) = \ln(\mathcal{T}_{test}/\mathcal{T}_0) - \ln(\mathcal{T}_{baseline}/\mathcal{T}_0)$, with $\mathcal{T}_{test}$ and $\mathcal{T}_{baseline}$ representing the transmission at the test and baseline partial hydrogen pressures, respectively. A more detailed discussion on this approach can be found in Ref. [34]. Once the response rate has been computed, we fit the obtained values to

a power law: $\text{Response Rate} = aP_{H_2}^{\gamma}$ where a is a constant and γ is the exponent. As established in refs. [34, 35, 51], $\gamma = 0.5$ suggests a diffusion-limited process, whereas an exponent of 1 points to a surface-limitation such as the hydrogen dissociation reaction.

Figure 6 provides the response rate analysis at −60 °C, suggesting that surface effects like hydrogen dissociation are the rate-limiting factor. We obtain $\gamma = 0.86 \pm 0.05$ for Ta, $\gamma = 0.90 \pm 0.11$ for $Ta_{88}Pd_{12}$, $\gamma = 0.85 \pm 0.10$ for $Ta_{88}Ru_{12}$, and $\gamma = 0.84 \pm 0.10$ for $Pd_{60}Au_{40}$. Although these gamma values indicate a predominant influence of surface effects as previously established at room temperature,[51] the deviation from 1 suggests a substantial role for diffusion. For the Ta-based samples, the value of $\gamma < 1$ could, for example, reflect sluggish diffusion through a thin $Pd_{60}Au_{40}$ capping layer (5 nm). This would be consistent with the much longer response times for the 20 nm $Pd_{60}Au_{40}$ sample (Figure 5) than for the Ta-based samples. Indeed, the activation energy for hydrogen diffusion in tantalum that crystallizes in a favorable bcc
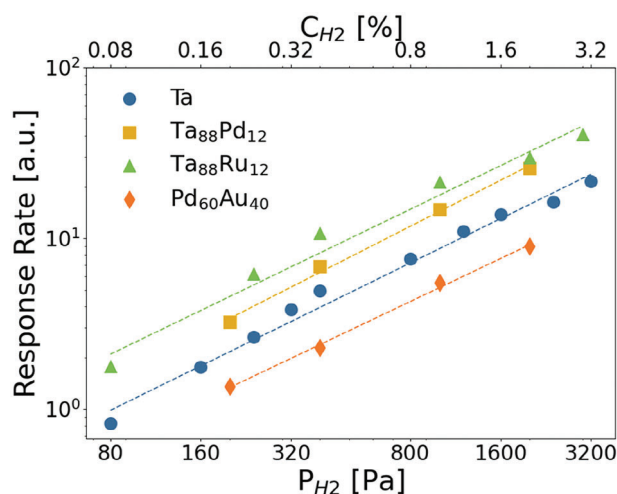

Figure 6. Response rate as a function of partial hydrogen pressure for Ta, $Ta_{88}Pd_{12}$, $Ta_{88}Ru_{12}$, and $Pd_{60}Au_{40}$ samples at −60 °C. The fitted power-law exponents are: Ta ($\gamma = 0.86 \pm 0.05$), $Ta_{88}Pd_{12}$ ($\gamma = 0.90 \pm 0.11$), $Ta_{88}Ru_{12}$ ($\gamma = 0.85 \pm 0.10$), and $Pd_{60}Au_{40}$ ($\gamma = 0.84 \pm 0.10$).

**ADVANCED
SCIENCE NEWS**

www.advancedsciencenews.com

**ADVANCED
FUNCTIONAL
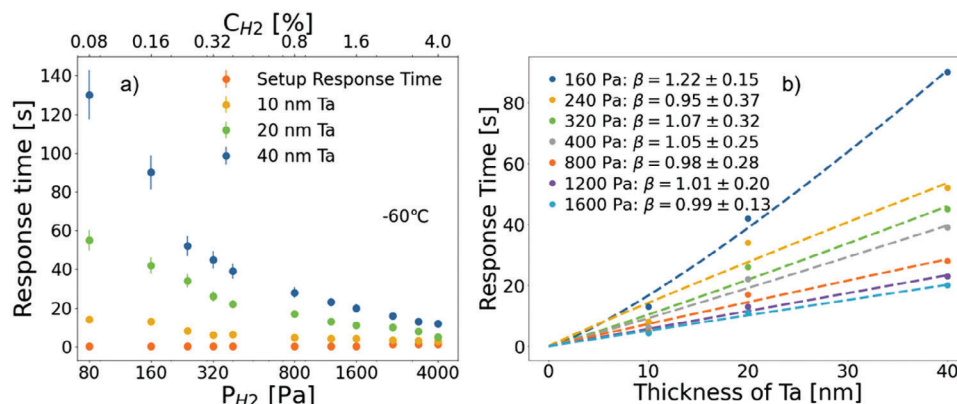MATERIALS**

www.afm-journal.de

Figure 7. a) Response times of 10, 20, and 40 nm Ta samples as a function of partial hydrogen pressure at −60 °C. b) Response time as a function of Ta sample thickness at different hydrogen partial pressures under −60 °C. The dashed lines indicate power-law fits with the fitted exponents (β) for each pressure.

structure (0.13 eV/atom) is considerably lower than for Pd that crystallizes in a fcc structure (0.23 eV/atom).[57,58]

As depicted in Figure S24 (Supporting Information), the response rate of hydrogen sensors is strongly influenced by temperature, exhibiting a higher response rate at higher temperatures for Ta and $Pd_{60}Au_{40}$ samples. Fitting of response rates to a power law indicates a predominant dissociation-limited process, particularly evident in the Ta samples, with exponent values of $\gamma \approx 1$ for $T \geqslant -30$ °C. Differently, for $T \geqslant -30$ °C the values seem to suggest for $Pd_{60}Au_{40}$ that diffusion still plays a role in determining the response time. The presence of the $Pd_{60}Au_{40}$ layer, serving as either a capping or sensing layer, inevitably influences the response kinetics of the Ta-based samples. Since the entire thin film system is tested as a whole, isolating the effect of the Ta layer is challenging.

To better delineate the rate-limiting processes in the Ta and Ta-based layers, we conducted a series of experiments on samples with a varying Ta layer thickness (10, 20, and 40 nm). As the 4 nm Ti adhesion, the 5 nm $Pd_{60}Au_{40}$, and PTFE layers are kept the same for all these samples, any thickness dependence should originate from the Ta layer. When the response times are completely limited by surface effects, we expect that the response times scale linearly with the thickness of the Ta sensing layer, i.e., $t_{90} \propto d_{Ta}$, as the number of hydrogen atoms that need to be dissociated and absorbed scales linearly with the layer thickness. Differently, when diffusion inside the Ta layer is rate-limiting, we expect, to a first approximation, that $t_{90} \propto d_{Ta}^2$. Indeed, the diffusion time is related to the mean square displacement: $t_{diffusion} \propto \langle x_{displ} \rangle^2$. As such, fitting a power law $t_{90} = a d_{Ta}^{\beta}$ to the data can help determining the rate-limiting step.

Figure 7a shows the response times for thin films with different Ta sensing layer thicknesses at various hydrogen concentrations. This, together with the scaling between the response time and the Ta layer thickness in Figure 7b, confirm that surface effects indeed primarily limit the response time. We find that the exponent $\beta \approx 1$ for almost all investigated hydrogen concentrations. This is expected for response times limited by surface effects and supports the conclusion based

on the scaling of the response rate with the partial hydrogen pressure.

Looking at the analysis of the response rates, which shows that the kinetics are predominantly surface-limited, we observe that to improve the response times of the sensor, it is most effective to consider surface effects which include both the dissociation of hydrogen as well as the diffusion of hydrogen through the catalytic PdAu layer. This could imply developing new coatings that can reduce the activation energy of the catalyst layer (e.g., through creating bonds with Pd) or consider changing the microstructure, morphology, or composition of the catalyst layer.[29,51,59] Naturally, one can also decrease the layer thickness of the hydrogen sensing layer, which implies that fewer hydrogen atoms need to be dissociated, however, this may come at the price of a reduced optical contrast and an associated reduction in the resolution of the sensor.

4. Conclusion

Our comprehensive investigation establishes that optical hydrogen sensors can be used to efficiently detect and quantify hydrogen at sub-zero temperatures down to −60 °C. In situ low temperature XRD measurements show no signs of any phase transitions, plastic deformation or hysteresis down to −60 °C when the sensing materials are exposed to a changing hydrogen concentration. This is reflected in the optical properties of the sensing materials, which show well-defined, reversible and stable steps in the optical transmission with changing hydrogen concentration. Although the optical changes with a changing hydrogen concentration become smaller with decreasing temperature, and thus the potential resolution of the sensing materials decreases, a sizable optical contrast remains down to −60 °C. This is particularly true for $Ta_{88}Ru_{12}$, which shows the highest optical contrast and shortest response time of 6 s at −60 °C amongst all considered samples. A detailed analysis of the response times and response rates illustrates that the response times are predominantly limited by surface effects, such as the hydrogen dissociation reaction. From a broader perspective, this research not only demonstrates the operational viability of metal hydride based hydrogen sensors

**ADVANCED
SCIENCE NEWS**

www.advancedsciencenews.com

**ADVANCED
FUNCTIONAL
MATERIALS**

www.afm-journal.de

in cold environments but also opens new avenues for their application.

Supporting Information

Supporting Information is available from the Wiley Online Library or from the author.

Conflict of Interest

Two of the authors are listed as inventor of the patent 'Optical thin-film hydrogen sensing material based on tantalum or other group V element alloy' owned by Delft University of Technology.

Data Availability Statement

The data that support the findings of this study are available from the corresponding author upon reasonable request.

[1] S. Li, E. Li, X. An, X. Hao, Z. Jiang, G. Guan, *Nanoscale* **2021**, *13*, 12788.
[2] N. Z. Muradov, T. N. Veziroğlu, *Int. J. Hydrogen Energy* **2008**, *33*, 6804.
[3] D. F. Dominković, I. Bačeković, A. S. Pedersen, G. Krajačić, *Renewable Sustainable Energy Rev.* **2018**, *82*, 1823.
[4] A. M. Abdalla, S. Hossain, O. B. Nisfindy, A. T. Azad, M. Dawood, A. K. Azad, *Energy Convers. Manage.* **2018**, *165*, 602.
[5] M. Sand, R. B. Skeie, M. Sandstad, S. Krishnan, G. Myhre, H. Bryant, R. Derwent, D. Hauglustaine, F. Paulot, M. Prather, D. Stevenson, *Commun. Earth Environ.* **2023**, *4*, 203.
[6] I. B. Ocko, S. P. Hamburg, *Atmos. Chem. Phys.* **2022**, *22*, 9349.
[7] C. Jia, L. Zhao, G. Huang, L. Liu, W. Wang, Y. Yang, Y. Miao, *Appl. Sci.* **2023**, *13*, 6869.
[8] E. Brauns, E. Morsbach, S. Kunz, M. Bäumer, W. Lang, *Sens. Actuators, B* **2014**, *193*, 895.
[9] L. Boon-Brett, J. Bousek, P. Moretto, *Int. J. Hydrogen Energy* **2009**, *34*, 562.
[10] F. Franke, S. Kazula, L. Enghardt, *J. Phys.: Conf. Series* **2023**, *2454*, 012001.
[11] T. Hübert, L. Boon-Brett, G. Black, U. Banach, *Sens. Actuators, B* **2011**, *157*, 329.
[12] E. Brauns, E. Morsbach, G. Schnurpfeil, M. Bäumer, W. Lang, *Sens. Actuators, B* **2013**, *187*, 420.
[13] I. Simon, M. Arndt, *Sens. Actuators, A* **2002**, *97*, 104.
[14] D. Berndt, J. Muggli, F. Wittwer, C. Langer, S. Heinrich, T. Knittel, R. Schreiner, *Sens. Actuators, A* **2020**, *305*, 111670.
[15] E. Miliutina, O. Guselnikova, S. Chufistova, Z. Kolska, R. Elashnikov, V. Burtsev, P. Postnikov, V. Svorcik, O. Lyutakov, *ACS Sens.* **2019**, *4*, 3133.
[16] Z. Li, M. Yang, J. Dai, G. Wang, C. Huang, J. Tang, W. Hu, H. Song, P. Huang, *Sens. Actuators, B* **2015**, *206*, 564.
[17] Z. Ye, H. Ruan, X. Hu, J. Dai, X. Luo, M. Yang, *Int. J. Hydrogen Energy* **2022**, *47*, 28204.
[18] L. Bannenberg, M. Heere, H. Benzidi, J. Montero, E. Dematteis, S. Suwarno, T. Jaroń, M. Winny, P. Orłowski, W. Wegner, L. J. Bannenberg, M. Heere, H. Benzidi, J. Montero, E. M. Dematteis, S. Suwarno, T. Jaroń, M. Winny, P. A. Orłowski, W. Wegner, A. Starobrat, K. J. Fijałkowski, W. Grochala, Z. Qian, J.-P. Bonnet, I. Nuta, W. Lohstroh, C. Zlotea, O. Mounkachi, F. Cuevas, et al., *Int. J. Hydrogen Energy* **2020**, *45*, 33687.
[19] L. J. Bannenberg, C. Boelsma, K. Asano, H. Schreuders, B. Dam, *J. Phys. Soc. Jpn.* **2020**, *89*, 051003.
[20] I. Darmadi, F. A. A. Nugroho, C. Langhammer, *ACS Sens.* **2020**, *5*, 3306.
[21] W.-T. Koo, H.-J. Cho, D.-H. Kim, Y. H. Kim, H. Shin, R. M. Penner, I.-D. Kim, *ACS nano* **2020**, *14*, 14284.
[22] K. Chen, D. Yuan, Y. Zhao, *Opt. Laser Technol.* **2021**, *137*, 106808.
[23] Z. Zhao, M. Carpenter, H. Xia, D. Welch, *Sens. Actuators, B* **2006**, *113*, 532.
[24] R. Westerwaal, J. Rooijmans, L. Leclercq, D. Gheorghe, T. Radeva, L. Mooij, T. Mak, L. Polak, M. Slaman, B. Dam, et al., *Int. J. Hydrogen Energy* **2013**, *38*, 4201.
[25] M. A. Butler, *Sens. Actuators, B* **1994**, *22*, 155.
[26] C. Wadell, F. A. A. Nugroho, E. Lidstrom, B. Iandolo, J. B. Wagner, C. Langhammer, *Nano Lett.* **2015**, *15*, 3563.
[27] F. A. A. Nugroho, I. Darmadi, V. P. Zhdanov, C. Langhammer, *ACS nano* **2018**, *12*, 9903.
[28] I. Darmadi, F. A. A. Nugroho, S. Kadkhodazadeh, J. B. Wagner, C. Langhammer, *ACS Sens.* **2019**, *4*, 1424.
[29] F. A. Nugroho, I. Darmadi, L. Cusinato, A. Susarrey-Arce, H. Schreuders, L. J. Bannenberg, A. B. da Silva Fanta, S. Kadkhodazadeh, J. B. Wagner, T. J. Antosiewicz, et al., *Nat. Mater.* **2019**, *18*, 489.
[30] L. J. Bannenberg, F. A. A. Nugroho, H. Schreuders, B. Norder, T. T. Trinh, N.-J. Steinke, A. A. Van Well, C. Langhammer, B. Dam, *ACS Appl. Mater. Interfaces* **2019**, *11*, 15489.
[31] L. J. Bannenberg, C. Boelsma, H. Schreuders, S. Francke, N. Steinke, A. Van Well, B. Dam, *Sens. Actuators, B* **2019**, *283*, 538.
[32] W. Ao, B. Xue, J. Dai, W. Hu, F. Zhang, M. Yang, *Opt. Mater.* **2024**, *152*, 115476.
[33] L. Bannenberg, H. Schreuders, B. Dam, *Adv. Funct. Mater.* **2021**, *31*, 2010483.
[34] L. J. Bannenberg, H. Schreuders, N. van Beugen, C. Kinane, S. Hall, B. Dam, *ACS Appl. Mater. Interfaces* **2023**, *15*, 8033.
[35] A. Borgschulte, R. Westerwaal, J. Rector, H. Schreuders, B. Dam, R. Griessen, *J. Catal.* **2006**, *239*, 263.
[36] S. Ohno, M. Wilde, K. Fukutani, *J. Chem. Phys.* **2014**, *140*, 13.
[37] M. Pozzo, D. Alfe, *Int. J. Hydrogen Energy* **2009**, *34*, 1922.
[38] A. Borgschulte, R. Gremaud, R. Griessen, *Phys. Rev. B: Condens. Matter Mater. Phys.* **2008**, *78*, 094106.
[39] P. W. Atkins, J. De Paula, J. Keeler, *Atkins' physical chemistry*, Oxford University Press, Oxford **2023**.
[40] Y. Fukai, *The metal-hydrogen system: basic bulk properties*, vol. *21*, Springer Science & Business Media, New York **2006**.

**ADVANCED
SCIENCE NEWS**

www.advancedsciencenews.com

**ADVANCED
FUNCTIONAL
MATERIALS**

www.afm-journal.de

[41] A. Pundt, R. Kirchheim, *Annu. Rev. Mater. Res.* **2006**, *36*, 555.

[42] V. Burlaka, S. Wagner, M. Hamm, A. Pundt, *Nano Lett.* **2016**, *16*, 6207.

[43] S. Wagner, P. Klose, V. Burlaka, K. Nörthemann, M. Hamm, A. Pundt, *ChemPhysChem* **2019**, *20*, 1890.

[44] X. Xin, G. K. Pálsson, M. Wolff, B. Hjörvarsson, *Phys. Rev. Lett.* **2014**, *113*, 046103.

[45] T. B. Flanagan, W. A. Oates, in *Proceedings: EPRI-NSF Workshop on Anomalous Effects in Deuterided Metals*, Citeseer, Princeton, NJ **1991**.

[46] L. J. Bannenberg, L. Blom, K. Sakaki, K. Asano, H. Schreuders, *ACS Mater. Lett.* **2023**, *5*, 962.

[47] T. Schober, *Solid State Phenom.* **1996**, *49*, 357.

[48] L. J. Bannenberg, D. J. Verhoeff, N. Jonckers Newton, M. Thijs, H. Schreuders, *ACS Appl. Nano Mater.* **2024**, *7*, 1757.

[49] P. Ngene, R. J. Westerwaal, S. Sachdeva, W. Haije, L. C. P. M. de Smet, B. Dam, *Angew. Chem., Int. Ed.* **2014**, *53*, 12081.

[50] F. A. A. Nugroho, I. Darmadi, L. Cusinato, A. Susarrey-Arce, H. Schreuders, L. J. Bannenberg, A. B. da Silva Fanta, S. Kadkhodazadeh, J. B. Wagner, T. J. Antosiewicz, et al., *Nat. Mater.* **2019**, *18*, 489.

[51] L. J. Bannenberg, B. Boshuizen, F. A. Ardy Nugroho, H. Schreuders, *ACS Appl. Mater. Interfaces* **2021**, *13*, 52530.

[52] R. Delmelle, P. Ngene, B. Dam, D. Bleiner, A. Borgschulte, *ChemCatChem* **2016**, *8*, 1646.

[53] L. J. Bannenberg, M. Van Exter, M. N. Verleg, B. Boshuizen, S. R. Parnell, M. Thijs, H. Schreuders, *J. Neutron Res.* **2024**, *26*, 1.

[54] M. Björck, G. Andersson, *J. Appl. Crystallogr.* **2007**, *40*, 1174.

[55] A. Glavic, M. Björck, *J. Appl. Crystallogr.* **2022**, *55*, 1063.

[56] Z. S. Wang, G. R. Darling, S. Holloway, *J. Chem. Phys.* **2004**, *120*, 2923.

[57] P. Hornung, A. Khan, D. Torgeson, R. Barnes, *Zeitschrift für Physikalische Chemie* **1979**, *116*, 77.

[58] H. Kimizuka, S. Ogata, M. Shiga, *Phys. Rev. B* **2018**, *97*, 014102.

[59] D. Spirjakin, A. Baranov, S. Akbari, C. Phong, N. Tuan, in *2021 IEEE Sensors Applications Symposium (SAS)*, IEEE, Piscataway, NJ **2021**, pp. 1–5.